Appendix B

Supplementary Material for Chapter 4

B.1 Model Performance Details

B.1.1 SSL Incidence Model (Model A — XGBoost)

Table B.1: SSL incidence model performance comparison: v1 (lat/lon included) vs v2 (env-only).

Model version	Features	AUC (mean ± SD)	Notes
v1 (lat/lon included)	env + lat + lon	0.840 ± 0.044	Geographic proximity leakage; lat top feature (gain 0.183)
v2 (env-only)	env only	0.880 ± 0.039	Production model; no spatial leakage

The v1 model is retained as an upper-bound benchmark reflecting the strength of spatial autocorrelation in the training data. The 5–7% lower AUC of the env-only model reflects genuine held-out predictive performance without the benefit of proximate training echograms inflating the score.

B.1.2 SSL Subtype Model (Model B — XGBoost)

Table B.2: SSL subtype model performance (k=3).

Metric	Value
Cross-validated accuracy	0.682 ± 0.025
n training labels	504
k (clusters)	3
Silhouette score (k=3)	0.216
Silhouette score (k=2)	0.214

k=3 was selected over k=2 for ecological interpretability. The silhouette scores are comparable at k=2 and k=3 (0.214 vs. 0.216), and both improve substantially over k=4 (0.161). The k=2 solution merges the warm mesotrophic (C1) and warm oligotrophic (C2) subtypes into a single warm-water cluster (n=449), collapsing the distinction between strong-DVM and diffuse, largely non-migratory aggregations.

B.1.3 U-Net Segmentation

Table B.3: U-Net SSL segmentation model versions.

Version	Training masks	Val masks	Validation Dice	Notes
v1	52	—	0.68	Pilot; masks archived
v5 (production)	88	15	0.685	All v2 analysis uses v5; 7.77M parameters

The production U-Net (v005) was trained on 88 manually drawn masks and validated on 15 held-out masks. The architecture follows the standard encoder–decoder U-Net (Ronneberger et al. 2015) with input shape (B, 1, 160, 1440), representing normalised S_v (dB) in the 0–800 m depth window at 5 m $\times$ 1 min resolution. Output is a per-pixel probability map of the same shape; masks are binarised at a threshold of 0.5.

B.1.4 Label Audit and Mask Consolidation

After initial labeling of 1,451 echograms (563 SSL-positive), all SSL-positive echograms were subject to a systematic quality audit:

Label audit. All 563 initially SSL-positive echograms were reviewed against the trained U-Net predictions. Echograms where the U-Net confidently detected no SSL-like structure — and where re-inspection confirmed the original label was incorrect — were reclassified as SSL-absent. A total of 59 echograms were flagged as false positives and removed from the SSL-positive set, yielding a final label count of **504 SSL-positive echograms** (34.7% of 1,451).

Mask audit and revision. All U-Net–predicted masks for SSL-positive echograms were reviewed in a Flask-based visual audit tool. Masks were assessed for boundary accuracy, depth alignment, and spurious segmentation. Of 606 echograms for which U-Net predictions were available, 53 required manual correction; these were re-drawn using a canvas-based mask editor and saved as revised masks. Two additional SSL-positive echograms had no U-Net prediction and no human mask and were excluded from feature extraction.

Mask consolidation. A single consolidated mask was assembled for each of the 502 SSL-positive echograms with available masks, using the following priority hierarchy:

1. Revised masks (53 manually corrected; highest priority)
2. Original human masks (99 hand-drawn masks not requiring revision)
3. U-Net predictions binarised at 0.5 (350 echograms)

Table B.4: Consolidated mask source summary.

Source	n echograms	Notes
Revised (manual correction)	53	Overrides human and U-Net
Original human mask	99	Unchanged from original drawing
U-Net prediction (0.5 threshold)	350	Binarised probability map
Total	**502**	2 SSL-positive echograms excluded (no mask available)

B.1.5 SSL Mask Examples

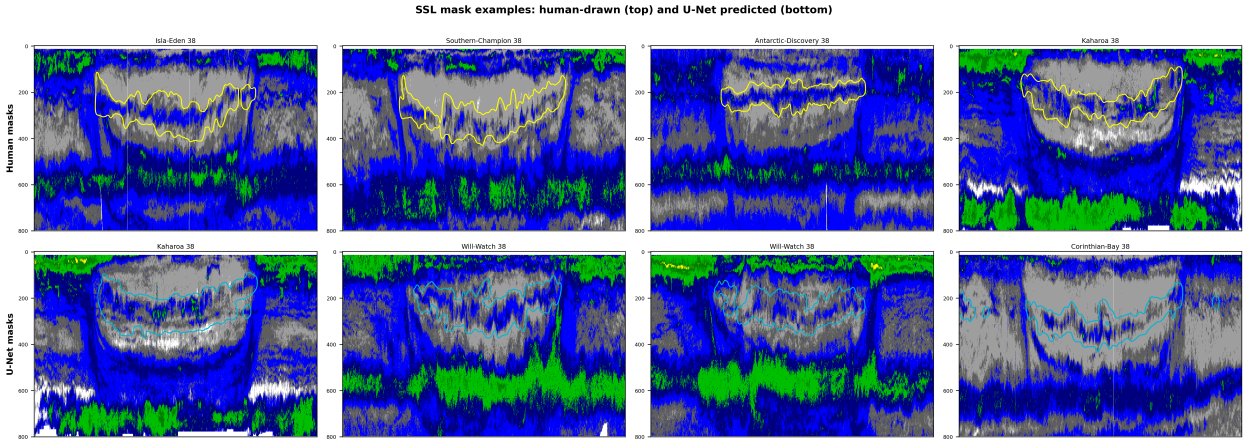

Figure B.1: Representative SSL mask examples. Top row: human-drawn mask boundaries (yellow contours) used for U-Net training. Bottom row: U-Net predicted mask boundaries (cerulean contours) from the production model (v005, Dice = 0.685). All echograms displayed over the 0–800 m depth range.

Table B.5: Environmental covariates co-located with each echogram. The V2 incidence model uses 9 features (marked ✓); additional covariates are retained for descriptive analysis but excluded from the model to avoid redundancy or spatial leakage.

Variable	**Source**	**Resolution**	**In V2 model**	**Description**
o2_surf (μmol kg^{-1})	WOA18 annual	1°	✓	Surface dissolved oxygen
omz_top_60_m (m)	WOA18 annual	1°	✓	Depth to 60 μmol kg^{-1} oxygen isoline
log(Chl-a)	MODIS-Aqua	4 km, 2018–2022 mean	✓	Log-transformed chlorophyll-a
SST (°C)	WOA18 annual	1°	✓	Sea surface temperature
Bathymetry (m)	ETOPO1	1′	✓	Seafloor depth
z_eu (m)	Derived	—	✓	Euphotic zone depth = $-\ln(0.01)/K_{d490}$
Lunar phase	Astronomical	—	✓	Phase (0–1) at date and longitude
MLD (m)	WOA18 annual	1°	✓	Mixed layer depth (0.5°C threshold)
K_{d490} (m^{-1})	MODIS-Aqua	4 km, 2018–2022 mean	✓	Diffuse attenuation coefficient
o2_200m (μmol kg^{-1})	WOA18 annual	1°	—	Dissolved oxygen at 200 m
Day length (h)	Astronomical	—	—	Excluded: deterministic function of latitude
predicted_dsl_wmd (m)	Aksnes 2017	—	—	Excluded: deterministic transform of K_{d490}
niche_gap_m (m)	Derived	—	—	Excluded: derived from z_eu and predicted_dsl_wmd

B.2 Environmental Covariate Table

Lat/lon were excluded from all model versions to avoid geographic proximity leakage (see Section B.1.1). Features ranked by V2 model importance (gain); see Fig. 4.3.

B.3 SSL Feature Extraction

A total of 18 acoustic and morphometric features were extracted from each consolidated mask and the corresponding echogram S_v field, spanning four functional categories. The 11 features used for clustering (Table 4.1) are a subset selected to remove highly correlated pairs (see Section 4.2.3). All 18 features and their computation are listed below for completeness. Features were standardized to zero mean and unit variance before clustering.

Notation. Let M_{dt} be the binary mask (1 = SSL, 0 = outside) at depth bin d and time column t. Let S_{dt} be S_v (dB) at (d, t). Let $L_t = \{d : M_{dt} = 1\}$ be the set of mask depth bins at column t. Let $S_{dt}^{\text{lin}} = 10^{S_{dt}/10}$ be linear S_v.

$\Delta z = 5$ m (vertical bin size). T = total number of time columns.

B.4 SSL Cluster Feature Statistics

B.5 Multi-frequency Differencing

Multi-frequency ΔS_v was computed within the SSL mask for all SSL-positive echograms with paired multi-frequency data: ΔS_v(38–18 kHz) (n=59), ΔS_v(38–70 kHz) (n=57), and ΔS_v(38–120 kHz) (n=90), spanning 8 vessels (Fig. B.2). ΔS_v(38–18) is the only pair that discriminates among clusters (Fig. 4.8 and Section 4.3.7). ΔS_v(38–70) and ΔS_v(38–120) are uniformly positive across all three clusters (+2.4 to +3.2 dB), confirming that gas-bearing scatterers contribute to SSL backscatter in all subtypes.

Table B.6: Feature definitions and computation.

Feature	Computation
mean_depth_m	$\bar{z} = \sum_{d,t} z_d \cdot S_{dt}^{\text{lin}} M_{dt} \;/\; \sum_{d,t} S_{dt}^{\text{lin}} M_{dt}$
vertical_extent_m	$\text{mean}_t\big(\max L_t - \min L_t\big)$
peak_sv_db	$\max_{d,t} S_{dt} M_{dt}$
nasc_mean	$\text{mean}_t \sum_{d \in L_t} S_{dt}^{\text{lin}} \cdot \Delta z$ (proportional to NASC)
temporal_coverage	$\lvert\{t : L_t \neq \varnothing\}\rvert \;/\; T$
boundary_depth_range_m	$\max_t \min L_t \;-\; \min_t \min L_t$
maxsv_depth_range_m	$\max_t z_t^\star - \min_t z_t^\star$, where $z_t^\star = z_{\arg\max_d S_{dt} M_{dt}}$
maxsv_depth_iqr_m	$Q_{75}(z_t^\star) - Q_{25}(z_t^\star)$
parabolic_curvature	Curvature of quadratic fit to $z_t^\star$
parabolic_r2	R^2 of that quadratic fit
energy_conc_20m	$\text{mean}_t \sum_d : \; \text{mean}_t\big(\sum_{d \in L_t} S_{dt}^{\text{lin}}\big)$ within 20 m of peak
erb_m	$\text{mean}_t\big(\sum_{d \in L_t} S_{dt}^{\text{lin}}\big) / \max_{d \in L_t} S_{dt}^{\text{lin}}$ (equivalent rectangular bandwidth)
bright_core_thickness_m	$\text{mean}_t\big\lvert\{d \in L_t : S_{dt} \geq \max_{d' \in L_t} S_{d't} - 3\}\big\rvert \cdot \Delta z$
peak_prominence_mean_db	$\text{mean}_t\big(\max_{d \in L_t} S_{dt} - \text{mean}_{d \in L_t} S_{dt}\big)$
peak_depth_autocorr_lag1	$\text{Corr}(z_t^\star,\; z_{t+1}^\star)$ (Pearson, lag 1 ping $\approx$ 1 min)
peak_depth_autocorr_lag10	$\text{Corr}(z_t^\star,\; z_{t+10}^\star)$ (lag 10 pings $\approx$ 10 min)
peak_sv_autocorr_lag1	$\text{Corr}\big(\max_{d \in L_t} S_{dt},\; \max_{d \in L_{t+1}} S_{d,t+1}\big)$
peak_streak_max	max length of consecutive run with peak S_v within 5 m of mode

Table B.7: Full feature statistics by SSL cluster (k=3), SSL-present echograms only. Values are means unless otherwise noted.

Feature	All SSL+	C0 subpolar	C1 mesotrophic	C2 oligotrophic
n	504	53	179	270
SSL depth (m)	245 ± 38	209	276	232
NASC_ssl (m^2 nmi^{-2})	—	196	35	58
SST (°C)	21.8	11.9	23.4	22.6
o2_surf (μmol kg^{-1})	225	—	—	—
ΔS_v (38–18 kHz, dB)	—	−1.8	+2.17	−0.7
DSL depth (m)	595	—	—	—
f_ssl (%)	4.3	11.6	2.9	3.7
MP_ssl (%)	18.3	34.4	22.6	12.2
Thermal savings (%)	37.6	16.3	35.0	43.2
Combined energetic benefit (%)	47.3	40.8	44.0	51.0

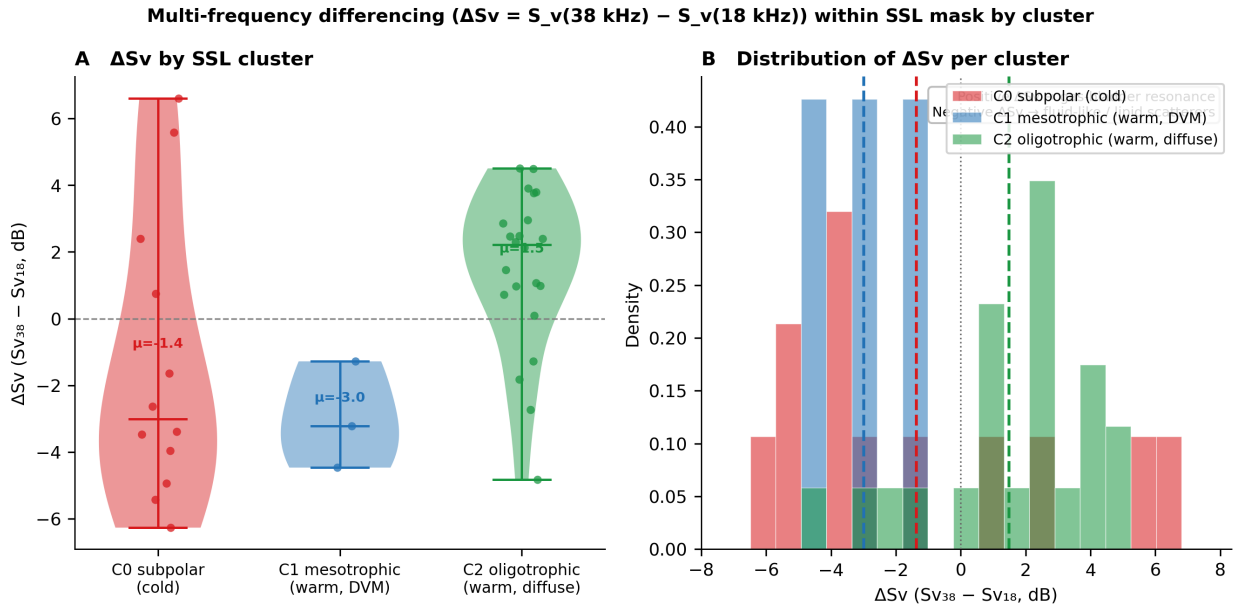

Figure B.2: Multi-frequency differencing (ΔS_v) within SSL masks by cluster for three frequency pairs. Violin plots show per-echogram distributions; horizontal bars indicate cluster means with 95% CI. Cluster colours: orange = C0 subpolar, blue = C1 mesotrophic, green = C2 oligotrophic.

B.6 Migration Fraction Methods

B.6.1 Per-echogram computation (this study)

For each SSL-positive echogram with a consolidated mask, the migration proportion (MP) framework of Klevjer et al. (Klevjer et al. 2016) was applied directly to the acoustic time series. All computations use the single-frequency 38 kHz echogram; NASC is computed by integrating S_v (linear units) over depth and averaging across pings within each time window.

Full mesopelagic MP. Daytime (08:00–16:00 local) and nighttime (22:00–04:00 local) NASC were computed over the full mesopelagic depth range (200–800 m). A diel normalisation ratio (DNR) — the median ratio of total water column S_v between day and night in SSL-absent echograms — was used to correct for diel changes in background scattering efficiency:

$$\mathrm{MP} = 1 - \frac{\mathrm{NASC}_{\mathrm{meso,night}} \times \mathrm{DNR}}{\mathrm{NASC}_{\mathrm{meso,day}}} \tag{B.1}$$

SSL-specific MP (MP_ssl). An SSL-specific migration proportion was computed using NASC within the SSL mask depth footprint, with peak-day (09:00–15:00) and peak-night (21:00–03:00) windows:

$$\mathrm{MP}_{\mathrm{ssl}} = 1 - \frac{\mathrm{NASC}_{\mathrm{mask,night}}}{\mathrm{NASC}_{\mathrm{mask,day}}} \tag{B.2}$$

SSL fraction of mesopelagic NASC ($f_$ssl). The fractional contribution of SSL backscatter to total mesopelagic backscatter was computed during peak daytime:

$$f\_\mathrm{ssl} = \frac{\mathrm{NASC}_{\mathrm{mask,day}}}{\mathrm{NASC}_{\mathrm{meso,day}}} \tag{B.3}$$

SSL center of mass. The S_v-weighted mean depth within the mask during peak daytime provides the effective carbon injection depth.

B.6.2 Carbon sequestration efficiency

Sequestration efficiency was evaluated using the Martin et al. (Martin et al. 1987) power-law flux attenuation, with exponent $b = 0.86$ and euphotic zone depth $z_{\mathrm{eu}} = 160$ m (mean over SSL-positive echograms):

$$F(z) \propto \left(\frac{z}{z_{\mathrm{eu}}}\right)^{-0.86} \tag{B.4}$$

Relative sequestration efficiency at the SSL injection depth (z_{ssl}) versus DSL injection depth (z_{dsl}) is:

$$\eta_{\mathrm{rel}} = \frac{F(z_{\mathrm{ssl}})}{F(z_{\mathrm{dsl}})} = \left(\frac{z_{\mathrm{ssl}}}{z_{\mathrm{dsl}}}\right)^{-0.86} \tag{B.5}$$

A value > 1 indicates that SSL-injected carbon is more efficiently returned to the atmosphere (less efficiently sequestered) relative to DSL-injected carbon.

B.6.3 Methods comparison

Key bias in prior methods. All prior methods underestimate the shallow-migrant fraction because they either ignore the SSL entirely or merge it with the DSL. The WMD method is negatively biased in SSL-present echograms: the SSL pulls daytime WMD shallower, reducing the apparent amplitude of the day–night centroid shift and underestimating DSL migration.

Limitations of this study's approach. The DNR correction assumes diel changes in total water column backscatter reflect calibration or behavioral efficiency effects rather than true biomass

Table B.8: Literature methods for estimating migrating proportion (MP) and their treatment of the SSL.

Method	Source	Metric	SSL treatment
Day/night NASC shift	Klevjer et al. 2016	MP = 1 − (NASC_night × DNR) / NASC_day	SSL not separated; included in total daytime NASC
WMD centroid shift	Bianchi et al. 2013 NGeo	MP ≈ 1 − WMD_night / WMD_day	SSL pulls WMD shallow → underestimates DSL migration
Isolume binary model	Bianchi et al. 2013 GBC	All below 10^{-3} W m^{-2} isolume migrate	SSL below isolume treated as migrants; no depth distinction
Trait-based MCE	Thibault et al. 2025	MCE = 0.5–1.25 × 10^{-2}	Crustacean group (100–500 m) overlaps SSL range but not distinguished
This study	—	Per-echogram MP_ssl (mask-bounded day/night NASC shift); f_ssl separately quantified	SSL explicitly resolved; MP_ssl and f_ssl computed per-echogram from consolidated masks

changes; this assumption may not hold in regions with strong advection. The SSL mask defines a depth footprint that may include non-SSL background scattering within the mask boundary, potentially inflating f_ssl and diluting MP_ssl estimates. The approach is limited to 38 kHz; multi-frequency methods would improve taxa-specific resolution of the migrant signal.

B.7 Carbon Flux Analysis: Computational Details

This section provides the equations underlying the exploratory carbon flux analysis presented in Section 4.3.7. Results and discussion are in the main text; only computational details are given here.

Full mesopelagic MP. Following Klevjer et al. (Klevjer et al. 2016):

$$\mathrm{MP} = 1 - \frac{s_{A\text{-M,night}} \times \mathrm{DNR}}{s_{A\text{-M,day}}} \tag{B.6}$$

where mesopelagic NASC ($s_{A\text{-M}}$) is integrated over 200–800 m, and the day-night ratio DNR = $s_{A\text{-T,day}}$ / $s_{A\text{-T,night}}$ normalizes for diel changes in total water column backscatter unrelated to vertical redistribution. Daytime and nighttime windows were defined as 08:00–16:00 and 22:00–04:00 local time respectively.

SSL-specific MP. MP_ssl was computed analogously using NASC within the SSL mask depth

footprint.

SSL fraction. $f\_\text{ssl} = \text{NASC}_{\text{ssl,day}}/\text{NASC}_{\text{meso,day}}$.

SSL injection depth. The Sv-weighted center-of-mass depth within the mask during peak daytime.

Sequestration efficiency. Evaluated using the Martin et al. (Martin et al. 1987) power-law:

$$F(z) \propto \left(\frac{z}{z_{\text{eu}}}\right)^{-0.86} \tag{B.7}$$

where $z_{\text{eu}} = 160$ m (mean euphotic depth for SSL-positive echograms).

Assumptions. This analysis uses NASC as a linear biomass proxy without taxon-specific target strength corrections, fixed day/night windows that do not account for latitude-dependent photoperiod, and assumes DNR conservation of total water column NASC between day and night.

B.8 Annotation Application

All manual annotation tasks — binary SSL labeling, pixel-wise mask drawing, mask quality audit, and mask revision — were performed using a consolidated web-based application built in Python (Flask). The application integrates four functional modes into a single interface with shared label persistence and mask versioning:

1. **Binary labeling mode** (Fig. B.4): Displays each echogram full-screen with an EK500 color scale. A gradient boosting machine (GBM) classifier trained at startup on existing labels provides real-time model predictions and confidence estimates, and prioritises the review queue toward echograms where the model disagrees with existing labels or has low confidence (active learning). Labels are persisted to a master CSV with source tracking and review timestamps.

2. **Mask drawing mode** (Fig. B.5): Provides a dual-canvas overlay for pixel-wise SSL boundary delineation. Tools include adjustable brush/eraser, rectangular selection, horizontal band fill, and depth-range clipping. Masks are saved as single-channel PNGs at grid resolution (1440 × 160 pixels) with automatic backup of previous versions.

3. **Batch audit mode**: Displays echograms in paginated 8×8 mosaic grids with U-Net prediction contours overlaid. Reviewers flag false-positive labels or poor-quality masks with a single click. Flagged items are logged to separate audit CSVs.

4. **Mask revision editor**: Loads existing masks (checking revised → human → U-Net prediction in priority order) and allows redrawing with the same canvas tools as the mask drawing mode. Revised masks are saved to a dedicated directory without overwriting originals.

A standalone version of the binary labeling mode was packaged for distribution to external subject-matter experts for inter-rater reliability assessment (Section 4.2.2). This version serves pre-rendered PNG echograms and requires only Python and Flask (no raw acoustic data or model dependencies).

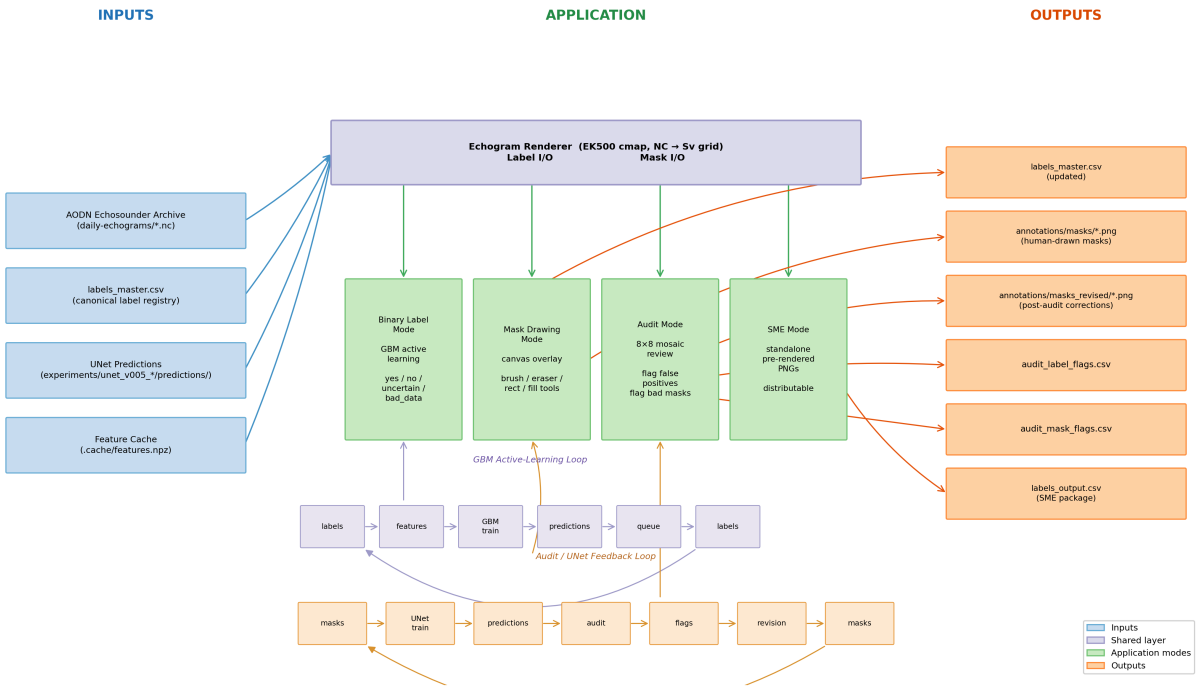

Figure B.3: Architecture of the consolidated annotation application showing data flow between the four functional modes, shared utilities, and annotation artifacts.

B.9 Seasonal SSL Habitat Predictions

To assess the sensitivity of SSL habitat predictions to seasonal variation in environmental covariates, we generated P(SSL) predictions using WOA18 seasonal climatologies (JFM, AMJ, JAS, OND) for SST, MLD, surface O_2, and OMZ depth, while retaining annual-mean values for Kd490, bathymetry, and lunar phase (which exhibit less seasonal variation). Seasonal predictions were generated using the V2 XGBoost incidence model (9 environmental features; Section 4.2.4).

Mean predicted P(SSL) across the Indo-Pacific grid varies modestly by season (AMJ: 0.434; JAS: 0.429; OND: 0.451; JFM: 0.459), reflecting the dominance of oxygen and OMZ structure — which

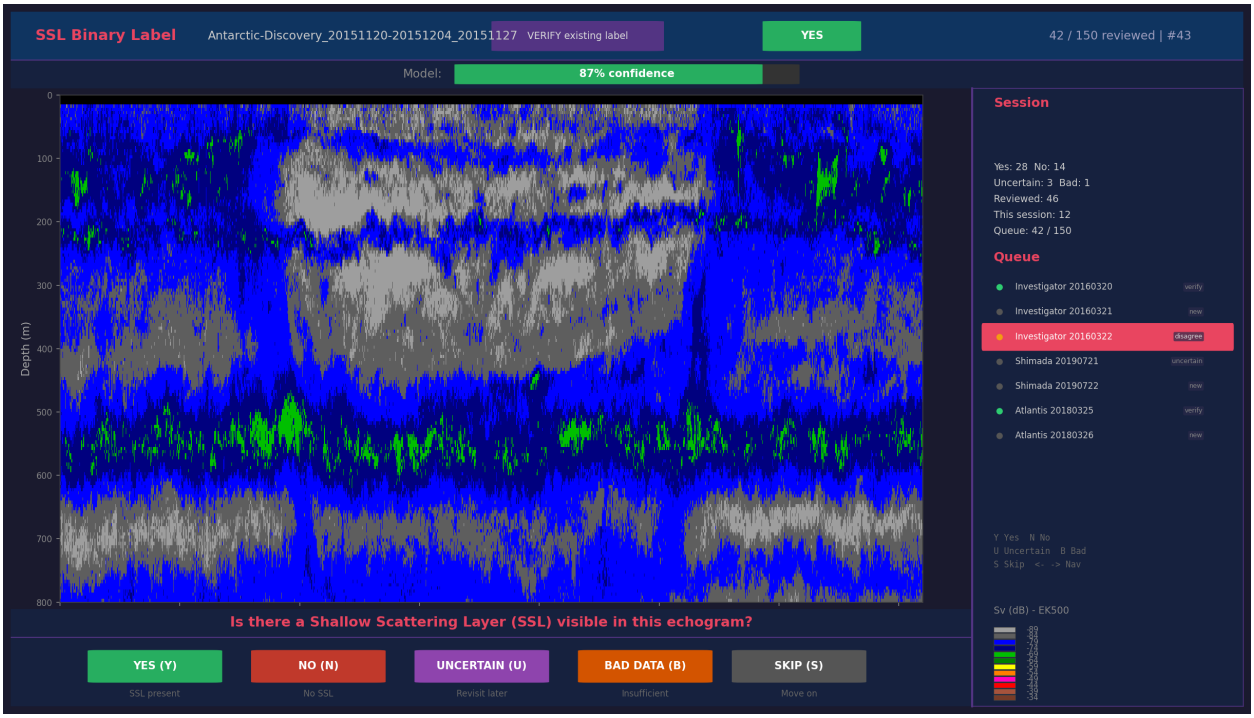

Figure B.4: Binary SSL labeling interface showing an echogram displayed in the EK500 color scale with model prediction confidence bar, label action buttons (Yes / No / Uncertain / Bad Data), and review queue sidebar.

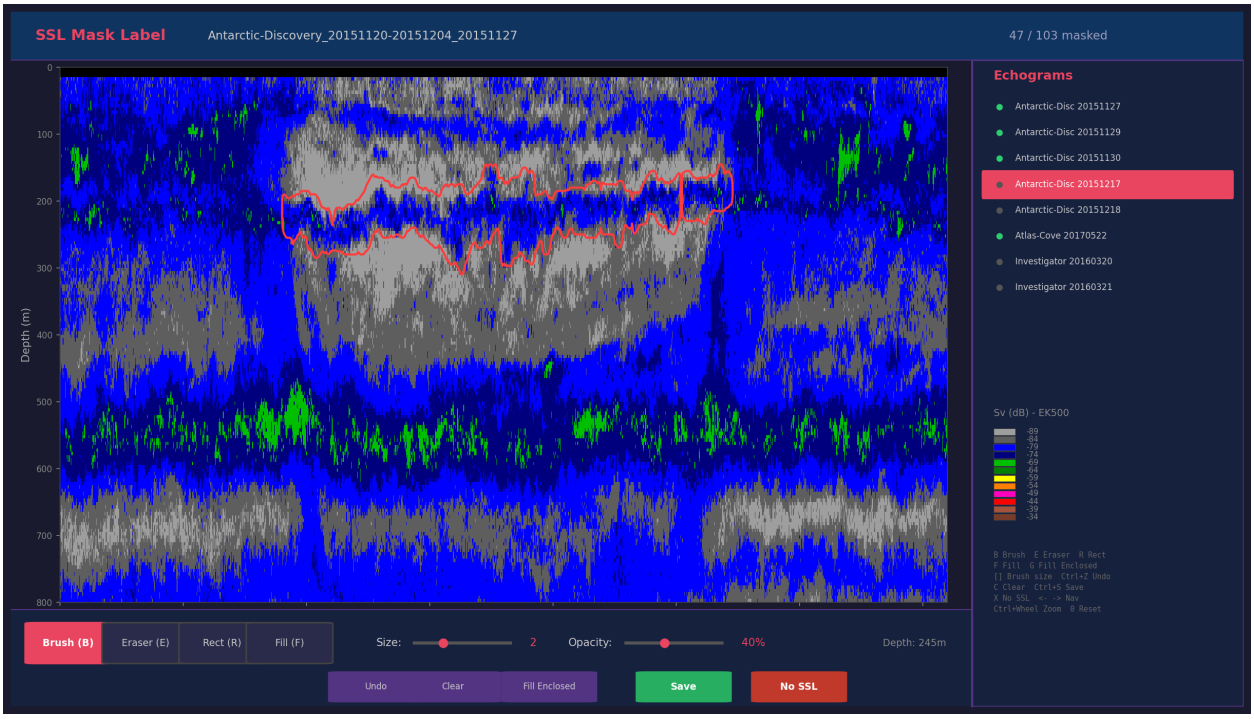

Figure B.5: Mask drawing interface showing an SSL-positive echogram with the annotation canvas overlay. The yellow contour indicates the hand-drawn SSL mask boundary.

are relatively stable seasonally — in the incidence model. The most pronounced seasonal differences occur at the poleward margins of the SSL habitat envelope, where SST and MLD vary strongly between summer and winter (Fig. B.6). This seasonal variation is consistent with the observation that SSL detections south of 40°S occur exclusively during the warmer months (Section 4.3.2), and provides context for the seasonal aliasing effect described in the main text.

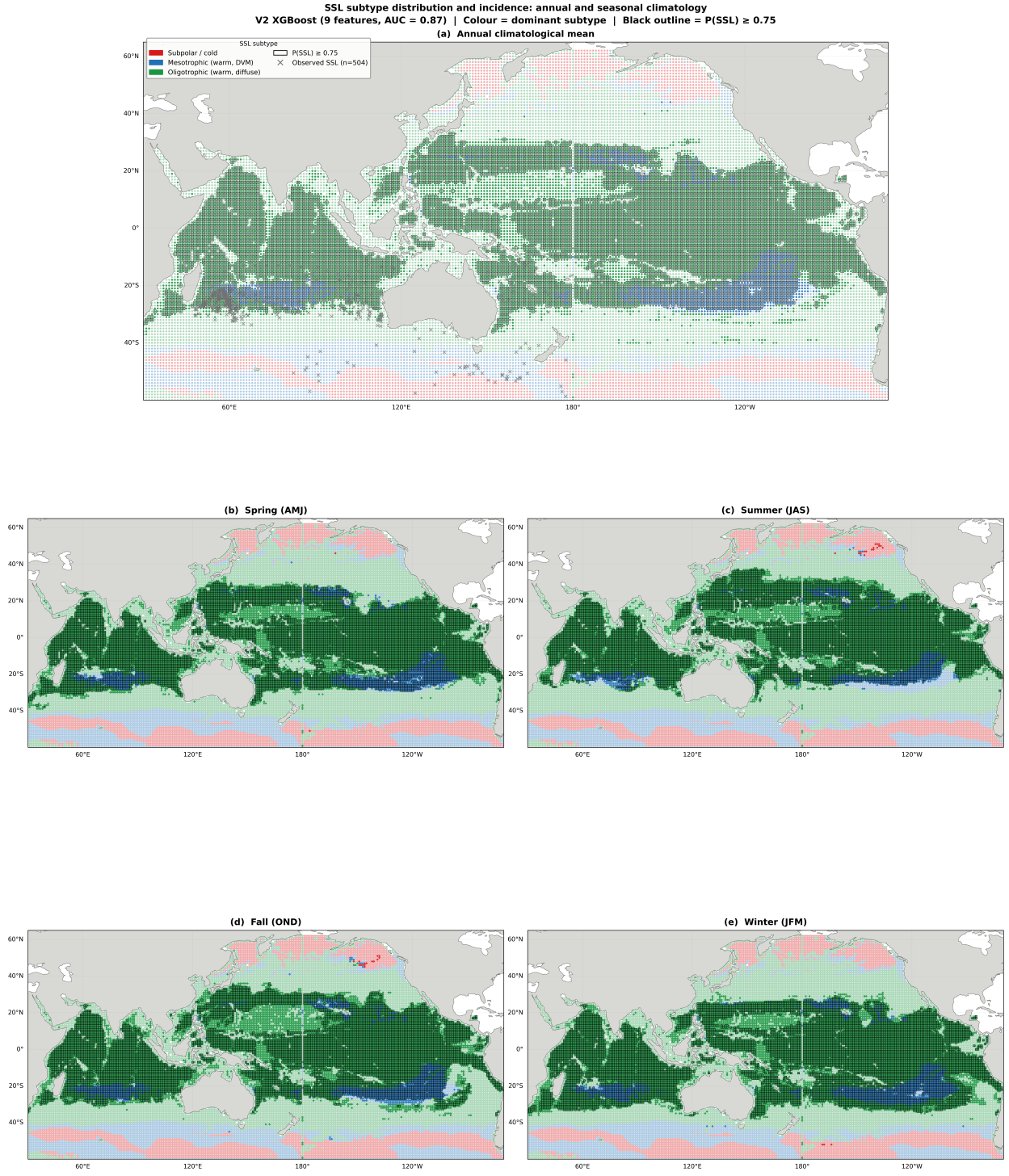

Figure B.6: Seasonal SSL subtype distribution and incidence predictions. Top panel: annual climatological mean (same as Fig. 4.1). Bottom four panels: seasonal predictions using WOA18 seasonal climatologies for SST, MLD, O_2, and OMZ depth. Colour indicates dominant predicted SSL subtype (green = oligotrophic; blue = mesotrophic; red = subpolar). Black contour: P(SSL) = 0.75.

Appendix C

Supplementary Material for Chapter 5

C.1 Hydrophone Recordings

Hydrophone recordings captured by the SoundTrap 600 during each comparison group's test runs confirmed the timing, repetition rate, and spectral content of both instruments' transmissions. Figure C.1 covers the A1 baseline comparison group, where the calibration sphere occupied the target position. Figure C.2 covers the dedicated hydrophone-as-target runs, where the hydrophone was moved to the target position for direct observation of each instrument's transmitted waveform.

C.2 Environmental Noise Floor Details

Low-frequency noise (< 10 kHz) was higher during daytime, as expected from mechanical and electrical sources, but sonar-band noise was unaffected.

C.3 Per-Group SNR Statistics (Empty-Region Method)

Table C.1 summarises per-ping SNR statistics using the within-ping empty-region noise gate (2.1–2.6 m). Figure C.6 shows the corresponding per-group SNR distributions.

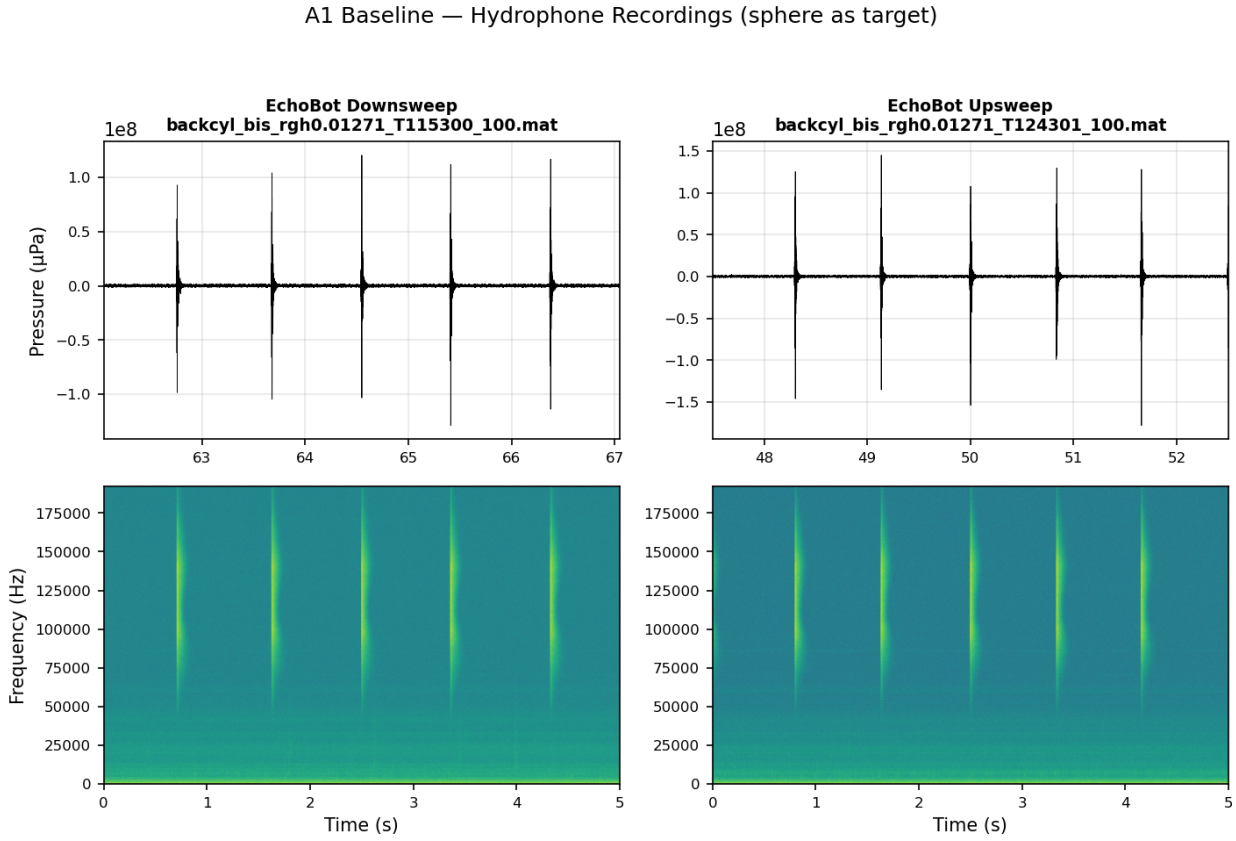

Figure C.1: A1 baseline — SoundTrap 600 hydrophone recordings during the A1 comparison group. EchoBot downsweep (left) and upsweep (right) pressure time series and spectrograms.

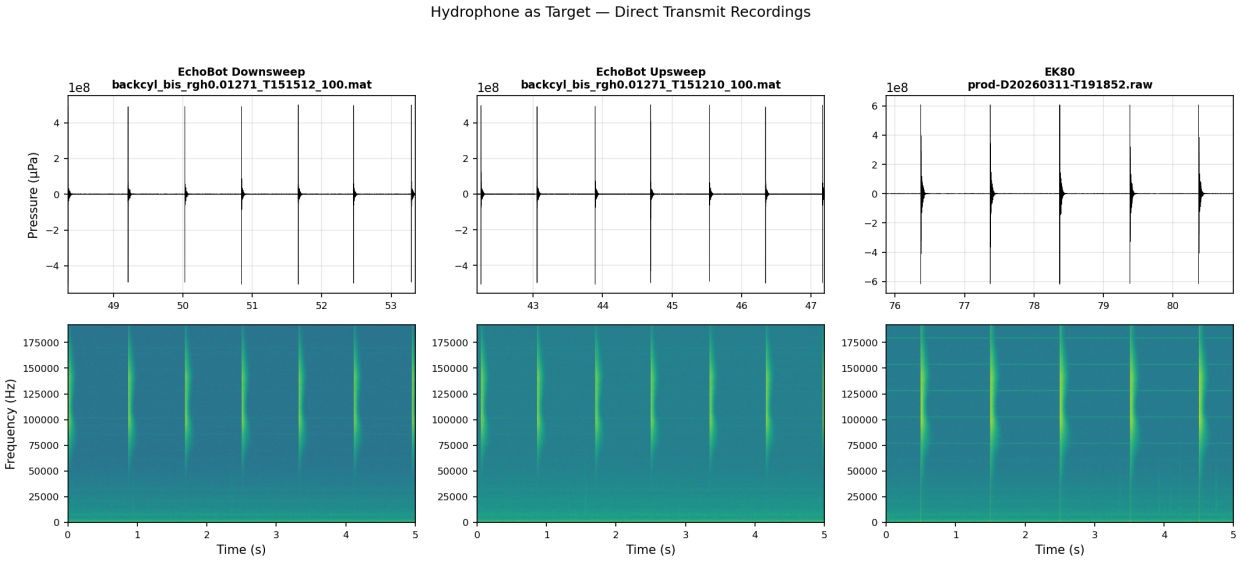

Figure C.2: Hydrophone as target — SoundTrap 600 recordings with the hydrophone at the target position. EchoBot downsweep, EchoBot upsweep, and EK80 pressure time series and spectrograms.

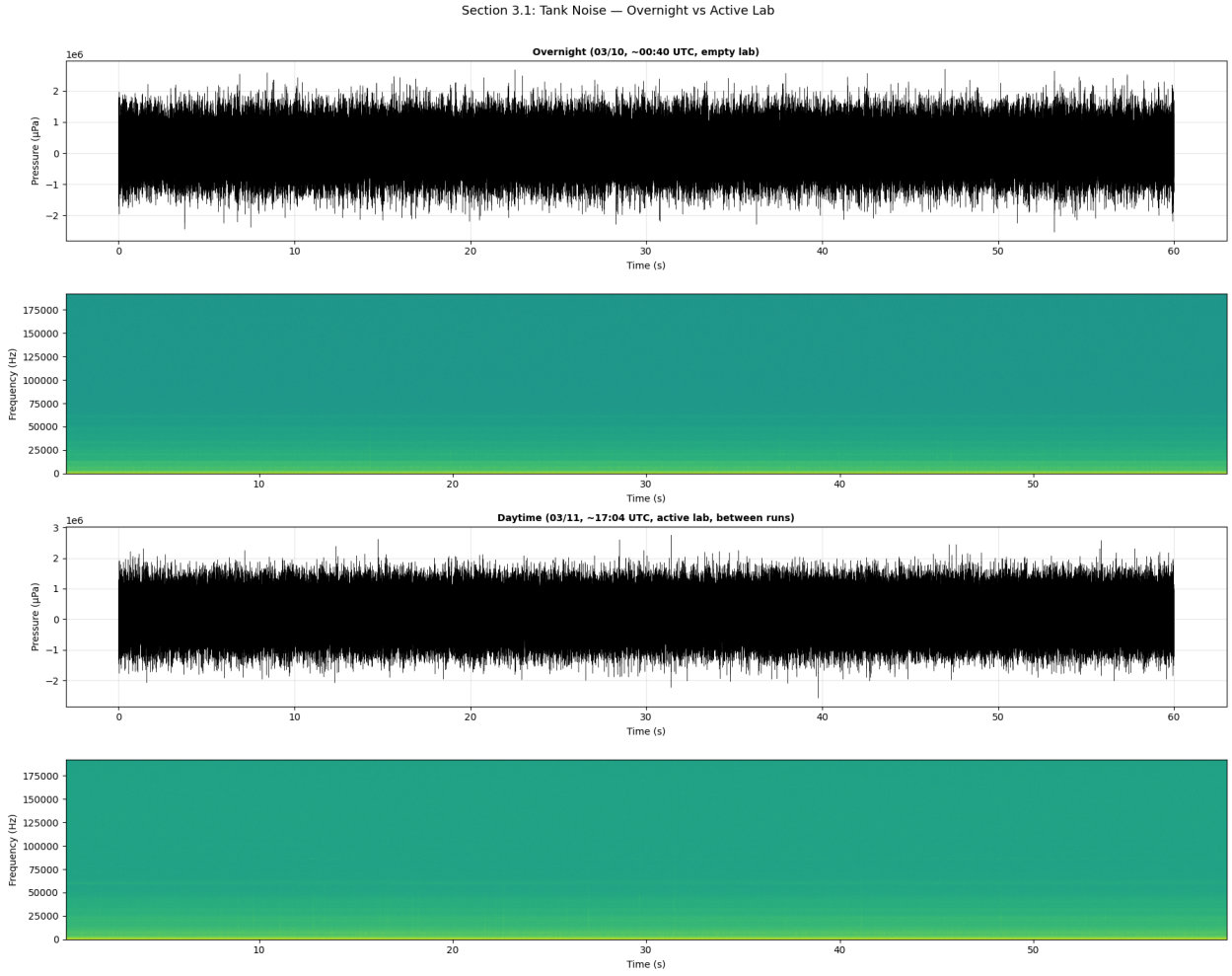

Figure C.3: Pressure time series and spectrograms.

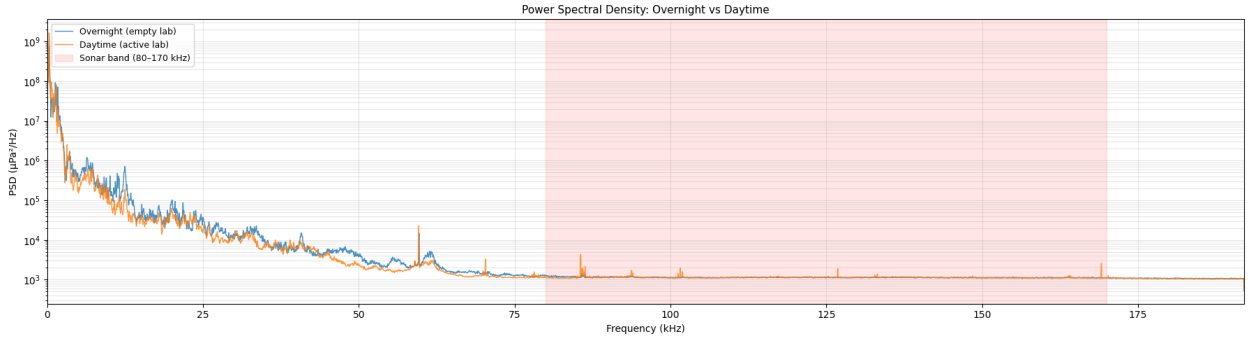

Figure C.4: PSD overlay with sonar band highlighted.

Figure C.5: Overnight versus daytime ambient noise comparison. (a) Pressure time series and spectrograms. (b) PSD overlay with sonar band highlighted.

Table C.1: Per-ping SNR statistics (mean ± std, in dB) using the within-ping empty-region noise gate (2.1–2.6 m).

Group	EK80 Target SNR	EB Down Target SNR	EB Up Target SNR
A1 (Baseline)	42.7 ± 0.20	46.7 ± 0.42	46.6 ± 0.49
A1-dup (Duplicate)	42.7 ± 0.20	46.8 ± 0.51	—
A1-rep (Late repeat)	42.7 ± 0.20	46.6 ± 0.45	46.6 ± 0.44
B1 (1.0 ms pulse)	34.6 ± 0.10	45.3 ± 0.27	38.8 ± 0.12
C1 (100–140 kHz)	39.0 ± 0.11	43.4 ± 0.40	43.3 ± 0.35
D1 (No target)	13.8 ± 3.69	17.7 ± 2.55	17.9 ± 2.29
P1-lo (Low power)	42.7 ± 0.20	45.3 ± 1.17	45.5 ± 1.02
P1-mid (Medium power)	42.7 ± 0.18	46.6 ± 0.45	46.6 ± 0.44
P1-hi (High power)	42.7 ± 0.15	47.0 ± 1.18	43.0 ± 0.58

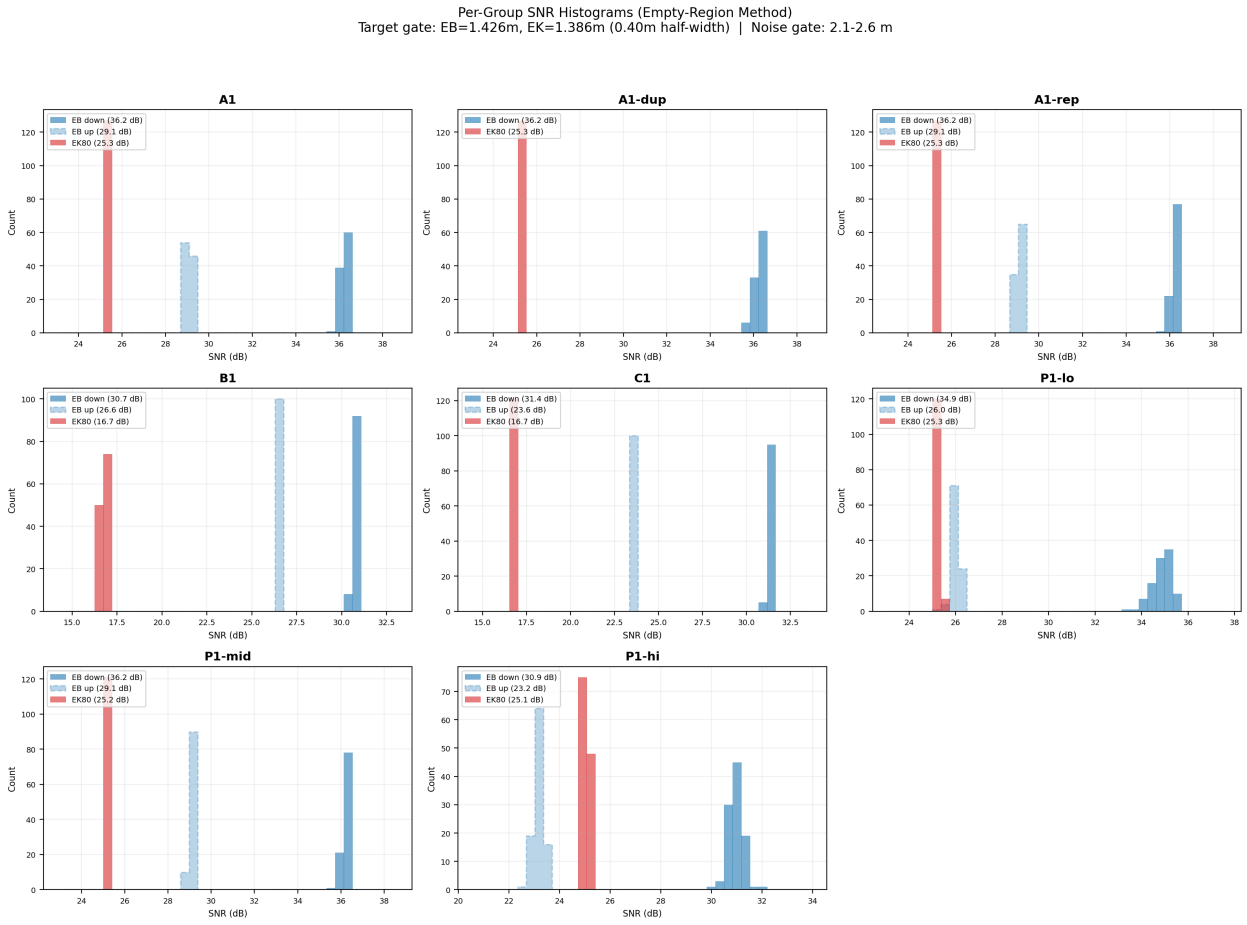

Figure C.6: Per-group SNR distributions using the empty water-column region (2.1–2.6 m) as within-ping noise reference.

C.4 Absolute TS(f) Comparison and Calibration Validation

The EK80 calibration pipeline was validated against the Simrad EK80 desktop software. For 15-ping TS@120 kHz comparison, the pipeline tracked the software read-by-read with a residual standard deviation of 0.013 dB and a mean offset of −0.54 dB. For 5-ping detailed TS(f) comparison across 9 frequencies, the mean residual was +0.02 dB (std 2.56 dB).

The calibrated EK80 TS(f) agrees with the NOAA theoretical curve to +2.4 dB at 120 kHz. EchoBot's uncalibrated TS(f) is offset by approximately +37 dB, representing the unknown electronics gain constant.

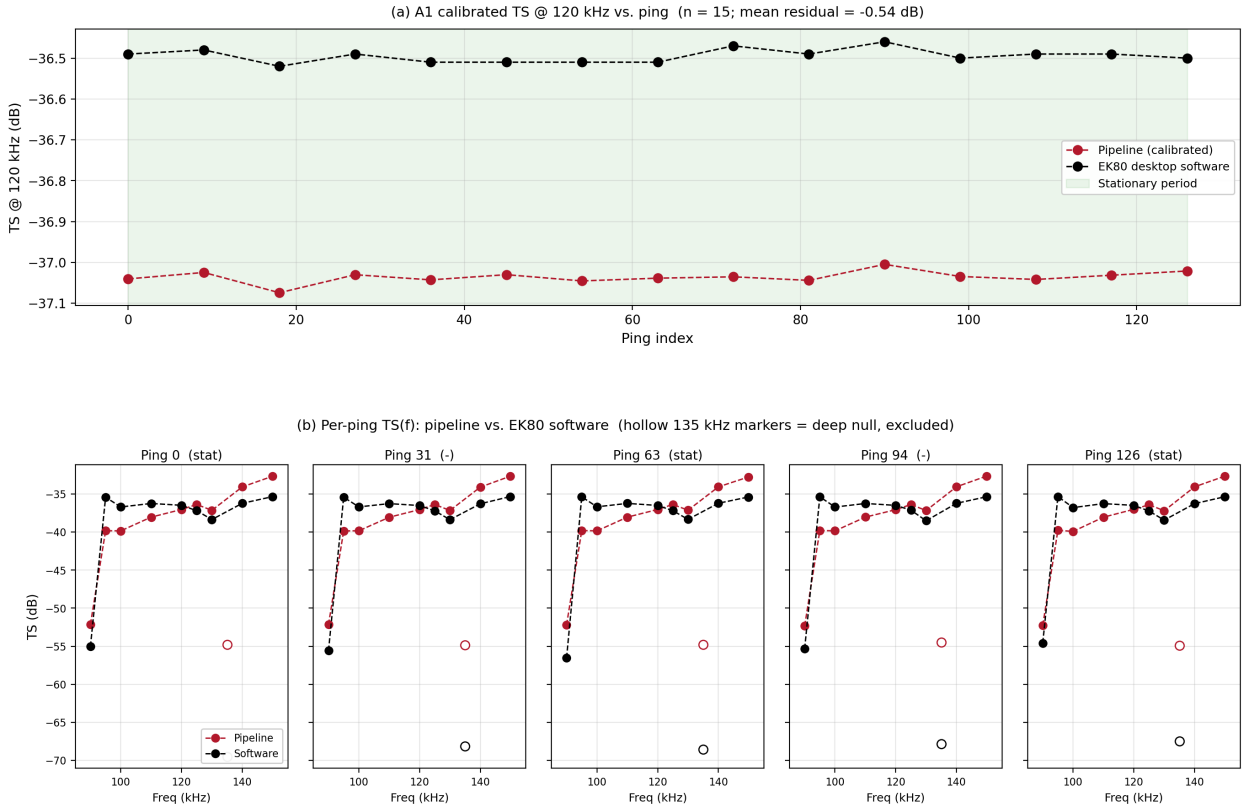

Figure C.7: EK80 pipeline calibration validated against the EK80 desktop software. (a) TS at 120 kHz for 15 pings. (b) Per-ping TS(f) at 10 frequencies.

C.5 EK80 Spectral TS(f) Pipeline: Detailed Implementation

The chirp replica was constructed by generating a linear FM sweep at the receiver sample rate (1500 kHz), applying a Hanning edge taper, and passing through the WBT (47-tap, 8× decimation)

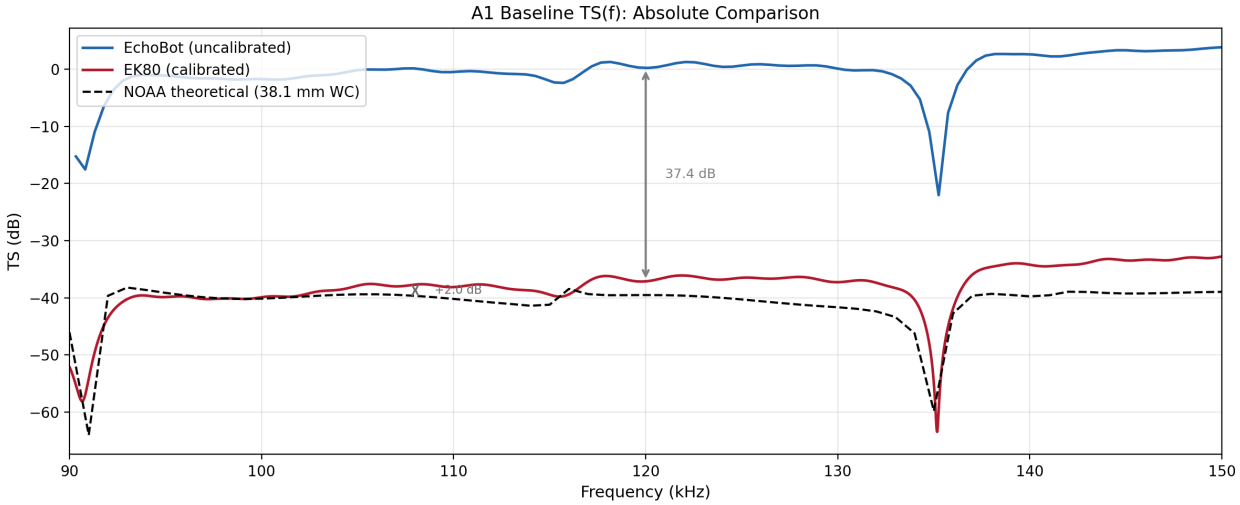

Figure C.8: A1 baseline TS(f) for EchoBot (uncalibrated, blue), EK80 (calibrated, red), and NOAA theoretical reference (black dashed). The ~37 dB offset represents the unknown EchoBot electronics gain constant.

and PC (91-tap, 2× decimation) filter chains extracted from the raw file, yielding a 96-sample complex baseband chirp replica at 93.75 kHz.

Pulse compression was performed by convolving each ping's mean-beam I/Q data with the time-reversed complex conjugate of the chirp replica, normalised by the chirp energy:

$$\mathrm{pc}[n] = \frac{1}{\|\mathbf{tx}_{\mathrm{filt}}\|^2} \sum_m x_{\mathrm{beam}}[m]\ \mathrm{conj}\big(\mathrm{mf}[m-n]\big) \tag{C.1}$$

where $\|\mathbf{tx}_{\mathrm{filt}}\|^2 = 44.24$. An aliasing-aware frequency mapping was applied:

$$f_{\mathrm{actual}} = f_{\mathrm{baseband}} + k\, f_{s,\mathrm{eff}} \tag{C.2}$$

The absolute TS(f) was computed via the full sonar equation:

$$\begin{aligned} \mathrm{TS}(f) = {} & 10\log_{10}\big|H(f)\big|^2 + 20\log_{10}\big(\|\mathbf{tx}_{\mathrm{filt}}\|^2\big) + Z_{\mathrm{dB}} \\ & + 40\log_{10}(R) + 2\alpha R - 10\log_{10}\left(\frac{\lambda(f)^2\, P_{\mathrm{tx}}}{16\pi^2}\right) \end{aligned} \tag{C.3}$$

where the impedance/beam correction is

$$Z_{\mathrm{dB}} = 10\log_{10}\left(\frac{N_{\mathrm{beams}}}{8}\right) + 20\log_{10}\left(\frac{|z_{er}+z_{et}|}{z_{er}}\right) - 10\log_{10}(z_{et}) \tag{C.4}$$

R is range, $\alpha = 0.04\,\text{dB/m}$ is the absorption coefficient, $\lambda(f) = c/f$ is the wavelength, $P_{\text{tx}} = 60\,\text{W}$ is the transmit power, and $G = 18.0\,\text{dB}$ is the transducer gain.

Bibliography

Aksnes, D. L., A. Røstad, S. Kaartvedt, et al. (2017). "Light penetration structures the deep acoustic scattering layers in the global ocean." In: *Science Advances* 3, e1602468.

Allken, V., N. O. Handegard, S. Rosen, et al. (2021). "A deep learning-based method to identify and count pelagic and mesopelagic fishes from trawl camera images." In: *ICES Journal of Marine Science* 78, pp. 3780–3792.

Archibald, K. M., D. A. Siegel, and S. C. Doney (2019). "Modeling the impact of zooplankton diel vertical migration on the carbon export flux of the biological pump." In: *Global Biogeochemical Cycles* 33, pp. 181–199.

Ariza, A., X. Irigoien, R. Proud, et al. (2023). "Acoustic seascape partitioning through functional data analysis." In: *Journal of Biogeography* 50, pp. 1546–1560.

Ariza, A., C. Sassa, M. Takahashi, et al. (2022). "Global decline of pelagic fauna in a warmer ocean." In: *Nature Climate Change* 12, pp. 928–934.

Arostegui, M. C., P. Gaube, P. A. Woodworth-Jefcoats, and C. D. Braun (2020). "Pelagic thresher shark (*Alopias pelagicus*) foraging at shallow scattering layer depths in the Red Sea." In: *Marine Ecology Progress Series*.

Arostegui, M. C., M. R. Heithaus, Y. P. Papastamatiou, et al. (2023). "A shallow scattering layer structures the energy seascape of an open ocean predator." In: *Science Advances* 9, eadi8200.

Bassett, C., A. De Robertis, and R. Levine (2020). "Frequency- and depth-dependent target strength measurements of individual mesopelagic scatterers." In: *The Journal of the Acoustical Society of America* 148, EL153–EL158.

Behrenfeld, M. J., P. Gaube, A. Della Penna, et al. (2019). "Global satellite-observed daily vertical migrations of ocean animals." In: *Nature* 576, pp. 257–261.

Benoit-Bird, K. J., W. W. L. Au, R. E. Brainard, et al. (2009a). "Observations of two distinct sound scattering layers in Kona, Hawaii." In: *Deep Sea Research Part I* 56, pp. 347–365.

Benoit-Bird, K. J., W. W. L. Au, and D. W. Wisdom (2009b). "Nocturnal light and lunar cycle effects on diel migration of micronekton." In: *Limnology and Oceanography* 54, pp. 1789–1800.

Benoit-Bird, K. J. and G. L. Lawson (2016). "Ecological insights from pelagic habitats acquired using active acoustic techniques." In: *Annual Review of Marine Science* 8, pp. 463–490.

Bergstra, J. and Y. Bengio (2012). "Random search for hyper-parameter optimization." In: *Journal of Machine Learning Research* 13, pp. 281–305.

Bianchi, D., E. D. Galbraith, D. A. Carozza, et al. (2013). "Intensification of open-ocean oxygen depletion by vertically migrating animals." In: *Nature Geoscience* 6, pp. 545–548.

Bianchi, D. and K. A. S. Mislan (2016). "Global patterns of diel vertical migration times and velocities from acoustic data." In: *Limnology and Oceanography* 61, pp. 353–364.

Bottou, L., C. Cortes, J. S. Denker, et al. (1994). "Comparison of classifier methods: a case study in handwritten digit recognition." In: *Proceedings of the 12th IAPR International Conference on Pattern Recognition, Vol. 3—Signal Processing*. Los Alamitos: IEEE Computer Society, pp. 77–82.

Boyd, P. W., H. Claustre, M. Levy, D. A. Siegel, and T. Weber (2019). "Multi-faceted particle pumps drive carbon sequestration in the ocean." In: *Nature* 568, pp. 327–335.

Boyer, T. P. et al. (2019). *World Ocean Atlas 2018*. NOAA Atlas NESDIS 87.

Braun, C. D., A. S. Afonso, G. B. Skomal, et al. (2022). "The functional and ecological significance of deep diving by large marine predators." In: *Annual Review of Marine Science* 14, pp. 129–159.

Braun, C. D., P. Gaube, A. S. Afonso, et al. (2023). "Linking vertical movements of large pelagic predators with distribution patterns of biomass in the open ocean." In: *Proceedings of the National Academy of Sciences* 120, e2306357120.

Brautaset, O., E. Ona, R. J. Korneliussen, et al. (2020). "Acoustic classification in multifrequency echosounder data using deep convolutional neural networks." In: *ICES Journal of Marine Science* 77, pp. 1391–1400.

Brierley, A. S., M. A. Brandon, and J. L. Watkins (1998). "An assessment of the utility of an acoustic Doppler current profiler for biomass estimation." In: *Deep-Sea Research Part I* 45.9, pp. 1555–1573. DOI: 10.1016/S0967-0637(98)00012-0.

Brunet-Imbault, B., G. Lemineur, C. Chappard, R. Harba, and C.-L. Benhamou (2005). "A new anisotropy index on trabecular bone radiographic images using the fast Fourier transform." In: *BMC Medical Imaging* 5, p. 4.

Calinski, T. and J. Harabasz (1974). "A dendrite method for cluster analysis." In: *Communications in Statistics—Theory and Methods* 3, pp. 1–27.

Chen, T. and C. Guestrin (2016). "XGBoost: a scalable tree boosting system." In: *Proceedings of the 22nd ACM SIGKDD International Conference on Knowledge Discovery and Data Mining*. New York: ACM, pp. 785–794.

Choi, H. and S. Choi (2004). "Kernel isomap." In: *Electronics Letters* 40, pp. 1612–1613.

Chu, D. and T. K. Stanton (1998). "Application of pulse compression techniques to broadband acoustic scattering by live individual zooplankton." In: *The Journal of the Acoustical Society of America* 104.1, pp. 39–55.

Cisewski, B., A. S. Maurer, M. Kaufmann, et al. (2021). "Vertical migration of pelagic and mesopelagic scatterers from ADCP backscatter data in the southern Norwegian Sea." In: *Frontiers in Marine Science* 7, p. 542386.

Cotter, E., C. Bassett, and A. Lavery (2021a). "Classification of broadband target spectra in the mesopelagic using physics-informed machine learning." In: *The Journal of the Acoustical Society of America* 149, pp. 3889–3901.

Cotter, E., C. Bassett, and A. Lavery (2021b). "Comparison of mesopelagic organism abundance estimates using in situ target strength measurements and echo-counting techniques." In: *JASA Express Letters* 1, p. 044402.

Culhane, E., A. Della Penna, M. C. Arostegui, and C. D. Braun (2025). "SOOP-BA SSL regional signatures and biophysical interactions." In: *[Journal TBD]*. Title TBD.

Daoud, M. I., S. Aly, W. Al-Nuaimy, et al. (2019). "Content-based image retrieval for breast ultrasound images using convolutional autoencoders: a feasibility study." In: *2019 3rd International Conference on Bio-Engineering for Smart Technologies (BioSMART)*. Piscataway, NJ: IEEE, pp. 1–6.

Davies, D. L. and D. W. Bouldin (1979). "A cluster separation measure." In: *IEEE Transactions on Pattern Analysis and Machine Intelligence* 2, pp. 224–227.

Davison, P. C., D. M. Checkley, J. A. Koslow, and J. Barlow (2013). "Carbon export mediated by mesopelagic fishes in the northeast Pacific Ocean." In: *Progress in Oceanography* 116, pp. 14–30.

De Robertis, A., C. Bassett, L. N. Andersen, I. Wangen, S. Furnish, and M. Levine (2019). "Amplifier linearity accounts for discrepancies in echo-integration measurements from two widely used echosounders." In: *ICES Journal of Marine Science* 76, pp. 1882–1892.

Deines, K. L. (1999). "Backscatter estimation using broadband acoustic Doppler current profilers." In: *Proceedings of the IEEE Sixth Working Conference on Current Measurement (Cat. No. 99CH36331)*. Piscataway, NJ: IEEE, pp. 249–253.

Della Penna, A. and P. Gaube (2020). "Mesoscale eddies structure mesopelagic communities." In: *Frontiers in Marine Science* 7, p. 454.

Della Penna, A., P. Gaube, A. Mignot, et al. (2022). "The impact of a Southern Ocean cyclonic eddy on mesopelagic micronekton." In: *Journal of Geophysical Research: Oceans* 127, e2022JC018893.

Demer, D. A. et al. (2017). *2016 USA–Norway EK80 Workshop Report: Evaluation of a wideband echosounder for fisheries and marine ecosystem science*. Cooperative Research Report 336. ICES.

Diogoul, N., A. Bertrand, P. Brehmer, et al. (2026). "Multi-frequency acoustic signatures of shallow scattering layers across the Indo-Pacific." In: *Scientific Reports*. In press.

Domokos, R., M. P. Seki, J. J. Polovina, and D. R. Hawn (2023). "Acoustic characterization of the mesopelagic community in the central North Pacific." In: *Deep-Sea Research Part II* 206, p. 105209.

Dornan, T., S. Fielding, R. A. Saunders, et al. (2019). "Swimbladder morphology masks Southern Ocean mesopelagic fish biomass." In: *Proceedings of the Royal Society B* 286, p. 20190353.

Dornan, T., S. Fielding, R. A. Saunders, and M. J. Genner (2022). "Large mesopelagic fish biomass and trophic structure in the Scotia Sea, Southern Ocean." In: *Proceedings of the Royal Society B* 289, p. 20211781.

Downie, R. A. et al. (2026). "Sonophore: An autonomous acoustic platform to monitor pelagic ecosystem dynamics." Manuscript in review.

Duda, R. O., P. E. Hart, and D. G. Stork (2000). *Pattern Classification*. 2nd ed. New York: Wiley.

ECCO Consortium, I. Fukumori, O. Wang, I. Fenty, G. Forget, P. Heimbach, and R. M. Ponte (2021). *Synopsis of the ECCO Central Production Global Ocean and Sea-Ice State Estimate (Version 4 Release 4)*.

Firing, E. (1995). *Processing ADCP data with the CODAS software system, version 3.1*.

Flagg, C. N. and S. L. Smith (1989). "On the use of the acoustic Doppler current profiler to measure zooplankton abundance." In: *Deep-Sea Research Part A* 36.3, pp. 455–474. DOI: 10.1016/0198-0149(89)90047-2.

Francois, R. E. and G. R. Garrison (1982). "Sound absorption based on ocean measurements. Part II: boric acid contribution and equation for total absorption." In: *The Journal of the Acoustical Society of America* 72, pp. 1879–1890.

Friedlingstein, P., M. O'Sullivan, M. W. Jones, et al. (2023). "Global Carbon Budget 2023." In: *Earth System Science Data* 15, pp. 5301–5369.

Garcia, H. E., K. W. Weathers, I. V. Smolyar, et al. (2024). *World Ocean Atlas 2023, Volume 3: Dissolved Oxygen, Apparent Oxygen Utilization, Dissolved Oxygen Saturation, and 30-Year Climate Normal*.

Geary, R. C. (1954). "The contiguity ratio and statistical mapping." In: *The Incorporated Statistician* 5, pp. 115–146.

Geoffroy, M., R. Arnason, A. Majewski, et al. (2019). "Mesopelagic sound scattering layers of the high Arctic: seasonal variations in biomass, species assemblage, and trophic relationships." In: *Frontiers in Marine Science* 6, p. 364.

Gheller, C. and F. Vazza (2022). "Convolutional deep denoising autoencoders for radio astronomical images." In: *Monthly Notices of the Royal Astronomical Society* 509, pp. 990–1009.

Glorot, X., A. Bordes, and Y. Bengio (2011). "Deep sparse rectifier neural networks." In: *Proceedings of the Fourteenth International Conference on Artificial Intelligence and Statistics*. JMLR Workshop and Conference Proceedings, pp. 315–323.

Gondara, L. (2016). "Medical image denoising using convolutional denoising autoencoders." In: *IEEE 16th International Conference on Data Mining Workshops (ICDMW)*. IEEE, pp. 241–246.

Goodfellow, I., Y. Bengio, and A. Courville (2016). *Deep Learning*. Cambridge, MA: MIT Press.

Gorgues, T., O. Aumont, and L. Mémery (2019). "Simulated changes in the particulate carbon export flux in the North Atlantic Ocean: impact of the NAO on the biological pump." In: *Global Biogeochemical Cycles* 33, pp. 1353–1370.

Gostiaux, L. and H. van Haren (2010). "Extracting meaningful information from uncalibrated backscattered echo intensity data." In: *Journal of Atmospheric and Oceanic Technology* 27, pp. 943–949.

Haris, K. et al. (2021). *IMOS — Ships of Opportunity (SOOP) Bioacoustics Sub-Facility Manual*. Tech. rep. IMOS.

Hatcher, R. (2024). "Oceanography for Everyone: open-source oceanographic instrumentation." In: *Oceanography* 37.1, pp. 104–107.

Heywood, K. J., S. Scrope-Howe, and E. D. Barton (1991). "Estimation of zooplankton abundance from shipborne ADCP backscatter." In: *Deep-Sea Research Part A* 38.6, pp. 677–691. DOI: 10.1016/0198-0149(91)90006-2.

Hubert, L. and P. Arabie (1989). "Combinatorial data analysis: confirmatory comparisons between sets of matrices." In: *Applied Stochastic Models and Data Analysis* 5, pp. 273–325.

Irigoien, X., T. A. Klevjer, A. Røstad, et al. (2014). "Large mesopelagic fishes biomass and trophic efficiency in the open ocean." In: *Nature Communications* 5, p. 3271.

Izard, L., A. Ariza, N. Fonvieille, E. Goberville, V. Djian, A. Kristiansen, J.-B. Charrassin, and C. Cotté (2025a). "Large differences in the distribution of pelagic biomass as a result of sonar frequency choice." In: *Proceedings of the Royal Society B* 292, p. 20242991.

Izard, L., R. Kiko, A. Biastoch, et al. (2024). "Global distribution of zooplankton biomass estimated by in situ imaging and machine learning." In: *Frontiers in Marine Science* 11, p. 1242262.

Izard, L., N. Kinzer, K. Brase, et al. (2025b). "Global patterns in mesopelagic biomass: seasonal trends and potential drivers." In: *ICES Journal of Marine Science* 82, fsaf006.

Izard, L., D. Mouillot, T. Brochier, C. Lett, and D. Gaertner (2021). "Estimating the importance of mesopelagic fish resonance scattering to the global ocean 38 kHz backscatter." In: *ICES Journal of Marine Science* 78, pp. 3464–3475.

Kaartvedt, S., A. Røstad, and D. L. Aksnes (2012a). "Isn't the deep-water fauna of the mesopelagic zone properly understood?" In: *Progress in Oceanography* 101, pp. 1–3.

Kaartvedt, S., A. Røstad, S. Christiansen, and T. A. Klevjer (2019). "Diel vertical migration and individual behavior of nekton beyond the ocean's twilight zone." In: *Deep-Sea Research Part I* 160, p. 103280.

Kaartvedt, S., A. Staby, and D. L. Aksnes (2012b). "Efficient trawl avoidance by mesopelagic fishes causes large underestimation of their biomass." In: *Marine Ecology Progress Series* 456, pp. 1–6.

Kingma, D. P. and J. Ba (2015). "Adam: a method for stochastic optimization." In: *Proceedings of the 3rd International Conference on Learning Representations (ICLR 2015)*.

Klevjer, T. A., X. Irigoien, A. Røstad, et al. (2016). "Large scale patterns in vertical distribution and behaviour of mesopelagic scattering layers." In: *Scientific Reports* 6, p. 19873.

Klevjer, T. A., W. Melle, T. Knutsen, et al. (2020). "Vertical distribution and migration of mesopelagic scatterers in four North Atlantic basins." In: *Deep Sea Research Part II* 180, p. 104842.

Klevjer, T. A., D. J. Torres, and S. Kaartvedt (2012). "Distribution and diel vertical movements of mesopelagic scattering layers in the Red Sea." In: *Marine Biology* 159, pp. 1833–1841.

Landis, J. R. and G. G. Koch (1977). "The measurement of observer agreement for categorical data." In: *Biometrics* 33.1, pp. 159–174.

Langbehn, T. J. and D. L. Aksnes (2018). "Sea in sight — fish in sight? Modelling the effect of underwater irradiance on fish detection distance." In: *Progress in Oceanography* 167, pp. 76–82.

Lavery, A. C., D. Chu, and J. N. Moum (2010). "Measurements of acoustic scattering from zooplankton and oceanic microstructure using a broadband echosounder." In: *ICES Journal of Marine Science* 67.2, pp. 379–394.

LeCun, Y., L. Bottou, Y. Bengio, et al. (1998). "Gradient-based learning applied to document recognition." In: *Proceedings of the IEEE* 86, pp. 2278–2324.

Lee, H. and V. Staneva (2020). *Review of machine learning approaches in the bioacoustics of the marine environment*. arXiv: 2009.08187.

Lee, W.-J. et al. (2024). "Interoperable and scalable echosounder data processing with Echopype." In: *ICES Journal of Marine Science* 81.10, pp. 1941–1951.

Lee, K., T. Mukai, and D.-h. Kang (2004). "A method for ADCP backscatter estimation: data from the Yellow Sea and East China Sea." In: *Journal of Oceanography* 60, pp. 363–373.

Lee, Z., K. L. Carder, and R. A. Arnone (2005). "Deriving inherent optical properties from water color: A multiband quasi-analytical algorithm for optically deep waters." In: *Applied Optics* 41, pp. 5755–5772.

Leung, S. W. (2020). "Particles, prey, and purse seines: a data-driven investigation into the impacts of climate on biological processes across the global ocean." PhD thesis. University of Washington.

Levine, R. M., C. Bassett, and A. De Robertis (2025). "Broadband and narrowband echosounder signals produce comparable estimates of volume backscattering." In: *ICES Journal of Marine Science* 82.9, fsaf160.

Locarnini, R. A., A. V. Mishonov, O. K. Baranova, et al. (2024). *World Ocean Atlas 2023, Volume 1: Temperature*.

Luo, B., R. C. Wilson, and E. R. Hancock (2003). "Spectral embedding of graphs." In: *Pattern Recognition* 36, pp. 2213–2230.

Mackenzie, K. V. (1981). "Nine-term equation for sound speed in the oceans." In: *The Journal of the Acoustical Society of America* 70, pp. 807–812.

Maclennan, D. N., P. G. Fernandes, and J. Dalen (2001). "A consistent approach to definitions and symbols in fisheries acoustics." In: *ICES Journal of Marine Science* 59, pp. 365–369.

MacQueen, J. (1967). “Multivariate observations.” In: *Proceedings of the 5th Berkeley Symposium on Mathematical Statistics and Probability, Vol. 1*. Berkeley, CA: University of California Press, pp. 281–297.

Mao, X., Q. Li, H. Xie, et al. (2016). “Least squares generative adversarial networks.” In: *Proceedings of the IEEE International Conference on Computer Vision (ICCV)*, pp. 2813–2821.

Martin, J. H., G. A. Knauer, D. M. Karl, and W. W. Broenkow (1987). “VERTEX: carbon cycling in the northeast Pacific.” In: *Deep-Sea Research* 34, pp. 267–285.

McMonagle, H., J. K. Llopiz, D. P. Nicholson, et al. (2023). “The biological carbon pump and global mesopelagic community structure.” In: *Annual Review of Marine Science* 15, pp. 121–156.

Mika, S., B. Schölkopf, A. Smola, et al. (1998). “Kernel PCA and de-noising in feature spaces.” In: *Advances in Neural Information Processing Systems*. Vol. 11, pp. 536–542.

Moran, P. A. P. (1948). “The interpretation of statistical maps.” In: *Journal of the Royal Statistical Society: Series B* 10, pp. 243–251.

Mullison, J. (2017). “Backscatter estimation using broadband acoustic Doppler current profilers – updated.” In: *Proceedings of the ASCE Hydraulic Measurements & Experimental Methods Conference*. Durham, NH, USA.

Norheim, E., T. A. Klevjer, and D. L. Aksnes (2016). “Evidence for light-controlled migration amplitude of a sound scattering layer in the Norwegian Sea.” In: *Marine Ecology Progress Series* 551, pp. 45–52.

Omand, M. M., D. K. Steinberg, and K. Stamieszkin (2021). “Clouds of particles in the ocean.” In: *Deep Sea Research Part II* 179, p. 104878.

Pena, M. and L. Calise (2016). “Use of ADCP backscatter data to estimate fish and zooplankton biomass.” In: *Deep Sea Research Part I* 108, pp. 37–48.

Perelman, J. N., Y. Ladroit, and P. C. Escobar-Flores (2023). “Mesoscale eddies modulate mixed layer depth and mesopelagic biomass and community structure.” In: *Deep Sea Research Part I* 200, p. 104133.

Pintelas, E., I. E. Livieris, and P. E. Pintelas (2021). “A convolutional autoencoder for tabular data.” In: *Applied Sciences* 11, p. 7735.

Proud, R., M. J. Cox, and A. S. Brierley (2017). “Biogeography of the global ocean’s mesopelagic zone.” In: *Current Biology* 27, pp. 113–119.

Proud, R., M. J. Cox, C. Le Guen, et al. (2018). “Fine-scale depth structure of pelagic communities throughout the global ocean based on acoustic sound scattering layers.” In: *Marine Ecology Progress Series* 598, pp. 35–48.

Proud, R., N. O. Handegard, R. J. Kloser, et al. (2019). “From siphonophores to deep scattering layers: uncertainty ranges for the estimation of global mesopelagic fish biomass.” In: *ICES Journal of Marine Science* 76, pp. 718–733.

Proud, R., W. J. F. Le Quesne, and A. S. Brierley (2020). “Estimating global mesopelagic fish biomass.” In: *Deep Sea Research Part I* 160, p. 103255.

Receveur, A., V. Allain, A. Lebourges-Dhaussy, et al. (2020a). “Micronekton distribution as a combination of its intermediate trophic position and physical environment: an approach from a passive acoustic perspective in the tropical Southwest Pacific.” In: *Deep-Sea Research Part II* 175, p. 104655.

Receveur, A., V. Allain, F. Ménard, et al. (2022). “Modelling marine predator habitat using the abundance of its pelagic prey in the tropical South-Western Pacific.” In: *Ecosystems* 25, pp. 757–779.

Receveur, A., E. Kestenare, V. Allain, et al. (2020b). "Biogeography of micronekton assemblages in the Natural Park of the Coral Sea." In: *Deep Sea Research Part I* 167, p. 103429.
Receveur, A., V. Smetacek, B. P. V. Hunt, et al. (2020c). "Micronekton distribution in the southwest Pacific (New Caledonia) inferred from shipboard-ADCP backscatter data." In: *Deep Sea Research Part I: Oceanographic Research Papers* 159, p. 103237.
Roemmich, D., J. Gilson, R. Davis, et al. (2009). "Decadal spinup of the South Pacific subtropical gyre." In: *Journal of Physical Oceanography* 39. See also Argo program: https://argo.ucsd.edu, pp. 1861–1877.
Ronneberger, O., P. Fischer, and T. Brox (2015). "U-Net: Convolutional networks for biomedical image segmentation." In: *MICCAI 2015*. Vol. 9351. LNCS, pp. 234–241.
Røstad, A., S. Kaartvedt, T. A. Klevjer, et al. (2016). "Fish are attracted to vessels." In: *ICES Journal of Marine Science* 63, pp. 1431–1437.
Rousseeuw, P. J. (1987). "Silhouettes: a graphical aid to the interpretation and validation of cluster analysis." In: *Journal of Computational and Applied Mathematics* 20, pp. 53–65.
Rumelhart, D. E., G. E. Hinton, and R. J. Williams (1986). "Learning representations by back-propagating errors." In: *Nature* 323, pp. 533–536.
Sabine, C. L., R. A. Feely, N. Gruber, et al. (2004). "The oceanic sink for anthropogenic CO_2." In: *Science* 305, pp. 367–371.
Sato, M. et al. (2024). *Mesopelagic community structure in upwelling ecoregions*.
Sato, M. and K. J. Benoit-Bird (2017). "Spatial variability of deep scattering layers shapes the Bahamian mesopelagic ecosystem." In: *Marine Ecology Progress Series* 580, pp. 69–82.
Sato, M., K. J. Benoit-Bird, J. K. Horne, et al. (2017). "Spatial and temporal variability of mesopelagic organisms in the California Current System." In: *Deep Sea Research Part II* 169, p. 104665.
Simmonds, J. and D. MacLennan (2008). *Fisheries Acoustics: Theory and Practice*. 2nd ed. Oxford: Blackwell Science.
Simmonds, J. and D. N. MacLennan (2005). *Fisheries Acoustics: Theory and Practice*. 2nd ed. Oxford: Blackwell Science.
Sobol, I. M. (1993). "Sensitivity estimates for nonlinear mathematical models." In: *Mathematical Modelling and Computational Experiments* 1.4, pp. 407–414.
Song, Y., C. Wang, and D. Sun (2022). "Both dissolved oxygen and chlorophyll explain the large-scale longitudinal variation of deep scattering layers in the tropical Pacific Ocean." In: *Frontiers in Marine Science* 9, p. 782032.
Sonnewald, M., S. Dutkiewicz, C. Hill, et al. (2020). "Elucidating ecological complexity: unsupervised learning determines global marine eco-provinces." In: *Science Advances* 6, eaay4740.
St. John, M. A., A. Borja, G. Chust, et al. (2016). "A dark hole in our understanding of marine ecosystems and their services: perspectives from the mesopelagic community." In: *Frontiers in Marine Science* 3, p. 31.
Stanton, T. K., D. Chu, J. M. Jech, and J. D. Irish (2010). "New broadband methods for resonance classification and high-resolution imagery of fish with swimbladders using a modified commercial broadband echosounder." In: *ICES Journal of Marine Science* 67, pp. 365–378.
Stanton, T. K., D. Chu, and P. H. Wiebe (1998). "Sound scattering by several zooplankton groups. II. Scattering models." In: *The Journal of the Acoustical Society of America* 103, pp. 236–253.
Steinberg, D. K. and M. R. Landry (2017). "Zooplankton and the ocean carbon cycle." In: *Annual Review of Marine Science* 9, pp. 413–444.

Steinley, D. (2004). “Properties of the Hubert–Arabie adjusted Rand index.” In: *Psychological Methods* 9, pp. 386–396.

Sutton, T. T., M. R. Clark, D. C. Dunn, et al. (2017). “A global biogeographic classification of the mesopelagic zone.” In: *Deep Sea Research Part I* 126, pp. 85–102.

Teledyne RD Instruments (1998). *ADCP acoustic Doppler current profiler: Principles of operation—a practical primer*. Field Service Technical Paper FST-003. Teledyne RD Instruments.

Thibault, M., R. Proud, D. Gascuel, et al. (2025). “Climate-driven mesopelagic biomass changes and implications for sustainable fisheries.” In: *ICES Journal of Marine Science* 82, fsaf023.

Urmy, S. S. and K. J. Benoit-Bird (2021). “Fear dynamically structures the ocean’s pelagic zone.” In: *Current Biology* 31, pp. 5086–5092.

Urmy, S. S., J. K. Horne, and D. H. Barbee (2012). “Measuring the vertical distributional variability of pelagic fauna in Monterey Bay.” In: *ICES Journal of Marine Science* 69, pp. 184–196.

Wang, X., X. Zhang, Y. Liu, et al. (2014). *Regional studies of shallow scattering layers*.

Wang, Z., A. C. Bovik, H. R. Sheikh, et al. (2004). “Image quality assessment: from error visibility to structural similarity.” In: *IEEE Transactions on Image Processing* 13, pp. 600–612.

Wiebe, P. H., G. L. Lawson, and A. C. Lavery (2023). “Acoustic estimates of macrozooplankton abundance and density for the mesopelagic zone.” In: *Deep Sea Research Part II* 206, p. 105224.

Willis, C. S. R., C. D. Braun, M. C. Arostegui, et al. (2024). “Large pelagic fishes are important components of the mesopelagic food web.” In: *Proceedings of the National Academy of Sciences* 121, e2306847121.

Wunsch, C. (2006). *Discrete Inverse and State Estimation Problems: With Geophysical Fluid Applications*. Cambridge: Cambridge University Press.

Yoerger, D. R. et al. (2021). “A hybrid underwater robot for multidisciplinary investigation of the ocean twilight zone.” In: *Science Robotics* 6.55, eabe1901.